Cement and Concrete Composites 90 (2018) 100–107

Contents lists available at ScienceDirect

Cement and Concrete Composites

journal homepage: www.elsevier.com/locate/cemconcomp

Ternary binder made of CFBC fly ash, conventional fly ash, and calcium hydroxide: Phase and strength evolution

Petr Hlaváček [a, *], Rostislav Šulc [a], Vít Šmilauer [a, **], Christiane Rößler [b], Roman Snop [c]

[a] Faculty of Civil Engineering, Czech Technical University in Prague, Thákurova 7, 166 29 Prague 6, Czech Republic
[b] F.A. Finger Institut für Baustoffkunde, Bauhaus-Universität Weimar, Coudraystraße 11, 99421 Weimar, Germany
[c] ČEZ Energetické produkty, s.r.o., Komenského 534, 253 01 Hostivice, Czech Republic

ARTICLE INFO

Article history:
Received 30 September 2015
Received in revised form
8 September 2017
Accepted 12 September 2017
Available online 15 March 2018

Keywords:
CFBC fly ash
Phase evolution
XRD
DTG
Mechanical properties
Micromechanical simulations

ABSTRACT

Coal combustion products present a source of aluminosilicate materials for further utilization. The ternary binder studied here is such an example, consisting of circulating fluidized bed combustion (CFBC) fly ash, conventional fly ash and $Ca(OH)^2$ activator. The paste yields a compressive strength of 32 MPa after 28 days of standard sealed curing. Volumetric evolution of crystalline and amorphous phases during hydration is quantified using XRD analysis, differential thermal gravimetry, porosimetry and electron microscopy. A micromechanical model is applied to interpret the evolution of compressive strength due to the growing proportions of C-S-H and ettringite in the system. This opens the way for further optimization and utilization of this ternary binder.

1. Introduction

Circulating fluidized bed combustion (CFBC) is a widely used technique to reduce SO_2 and NO_xemissions in coal-burning thermal power plants. The sulfur-containing coal is burned together with limestone so that the SO_2 emissions are in-situ transformed to anhydrous $CaSO_4$ [1–3]. Since the SO_2 is captured directly in the furnace, no wet scrubber of exhaust gases is needed to be installed separately and no waste gypsum is produced. The first CFBC boilers were installed in the 1970's able to process a wide range of fuel quality, high-moisture fuels or high-ash fuels [4–6]. The yearly production of CFBC fly ashes in the Czech Republic is about 0.5 million tons (2012) with a growing tendency.

Compared to conventional thermal power plants, where the combustion of pulverized coal runs under temperatures between 1200 and 1700°C, the CFBC boilers operate under temperatures around 850°C. The CFBC fly ash particles are therefore, on the contrary to the conventional fly ashes, unsintered (see Fig. 1) and their reactivity is considerably higher. On the other hand, the CFBC fly ashes contain about 11% of free lime and about 13.5% of gypsum anhydrite causing delayed formation of $Ca(OH)_2$, crystallization of ettringite and excessive expansion [7,8]. This prohibits addition of CFBC fly ashes to standard Portland-based cements and concretes and alternative utilizations are therefore sought.

To date, CFBC fly and bottom ashes have been used for geopolymer synthesis [9,10], production of autoclaved bricks [11], non-autoclaved aerated concretes [12], manufacturing of compressed earth bricks [13], and for preparation of self-cementing binders [14–16]. Armesto and Merino [17] studied differences between different coal combustion solid residues. They observed decreasing permeability of CFBC fly ash during leaching tests proving the hydraulic properties of the ash. Sheng et al. [18] distinguished three basic reactions during hydration of CFBC fly ash i) slaking of lime generating $Ca(OH)_2$, ii) generation of AFt and iii) formation of C-S-H gel. According to Li et al. [15], the main reaction products of CFBC fly ash hydration are C-S-H gel, ettringite and gypsum. Jewell et al. [19] studied fabrication of calcium sulfoaluminate-belite cements utilizing CFBC by-products. They found ettringite and C-S-H gel as the main hydration products of the CFBC incorporating cement.

This paper aims at quantification of the phases formed during

* Corresponding author.
** Corresponding author.
E-mail addresses: petr.hlavacek@fsv.cvut.cz (P. Hlaváček), rostislav.sulc@fsv.cvut.cz (R. Šulc), vit.smilauer@fsv.cvut.cz (V. Šmilauer), christiane.roessler@uni-weimar.de (C. Rößler), roman.snop@cez.cz (R. Snop).

https://doi.org/10.1016/j.cemconcomp.2017.09.020
0958-9465/

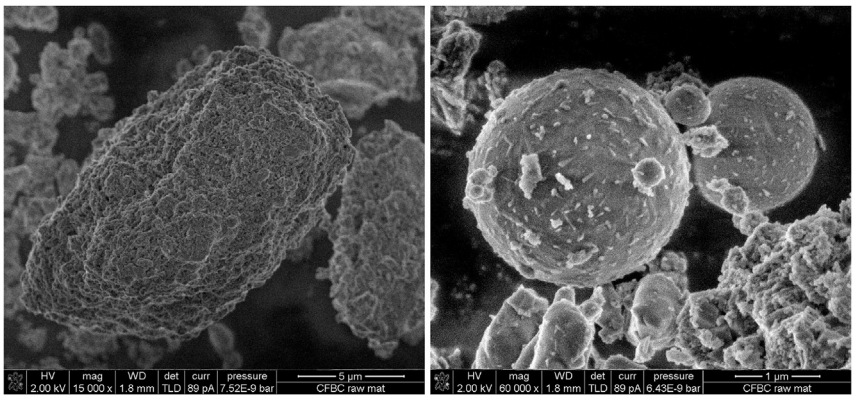

Fig. 1. CFBC fly ash particle (left) and a typical sintered sphere of ordinary fly ash (right). Images by Christiane Rößler, Weimar.

hydration of a CFBC fly ash-based ternary binder, followed with micromechanical prediction of compressive strength based on a multiscale model [20]. A model of volumetric phase evolution during hydration is based on XRD, differential thermal gravimetry (DTG) and porosimetry techniques, supported by an electron microscopy approach. The volumetric phase evolution is inspired by the works of Powers for ordinary Portland cement [21] and Šmilauer et al. for alkali activated materials [22]. The compressive strength of the hydrated CFBC fly ash paste is measured after 7, 14, 28 and 60 days of sealed hydration and compared with the micromechanically predicted data.

2. Materials and methods

CFBC fly ash from a circulating fluidized bed combustion power plant (d_{50} 36.3 µm, Blaine 603 m^2/kg) and conventional class F fly ash (FA) (d_{50} 44.9 µm, Blaine 484 m^2/kg) served as the raw materials. Commercially available calcium hydroxide is used as an alkali activator. Table 1 summarizes the chemical composition of the fly ashes and Fig. 2 depicts their particle size distributions. The XRD-identified phases on the raw materials are shown in Table 2.

All experiments were carried out at the level of paste. The mix composition was optimized for workability, maximal compressive strength at 28 days of curing and volumetric stability after an accelerated aging test (curing for an extra 28 days in 95°Cwater). The ratio between CFBC and conventional fly ash during the mixture optimization experiments varied from 0:1 to 1:0; the $Ca(OH)_2$ content remained constant. The 28 day compressive strength of 100% CFBC fly ash paste was found as 54 MPa, however it dropped by 30% after accelerated aging. The 100% conventional fly ash paste exhibits only 4 MPa after 28 days. The optimal composition was found as a mixture of 50% CFBC and 50% conventional fly ash. The optimized mix composition of the ternary binder (TB) is given in Table 3. A high range water-reducing admixture (superplasticizer) was added to reach a feasible workability with an acceptable water/binder ratio.

The mixing sequence started with 1 min of dry stirring to homogenize the source materials; addition of water; 10 min of mixing (285 rpm.); addition of the superplasticizer followed by another 5 min of mixing. The paste was subsequently cast into molds and vibrated for 2 min. Samples for determination of the phase evolution were ambient cured in sealed ampoules to prevent water evaporation and carbonation. After a given curing period (3, 7, 28 and 60 days) the hydration was stopped by water removal using acetone and a vacuum drying approach; the specimens were cut on a diamond saw to 3 mm slices, immersed in acetone for 24 h and vacuum dried for 48 h. Samples for the XRD and DTG analyses were ground in a laboratory small-scale planetary ball mill (Retsch PM 400). Beams for strength measurements were cast into 40 × 40 × 160 mm molds and covered by a foil to prevent water evaporation. After 7 days of sealed curing, the samples were unmolded and again wrapped in foil. The compressive strength was measured on half beams (≈ 40 × 40 × 80 mm) resulting from flexural strength measurements.

The XRD measurements were carried out by P. Bezdička, Institute of Inorganic Chemistry ASCR, on a PANalytical X PertPRO device using a CuKα X-ray tube. The Rietveld method was applied to obtain the mass fractions of crystalline phases with the help of ICSD

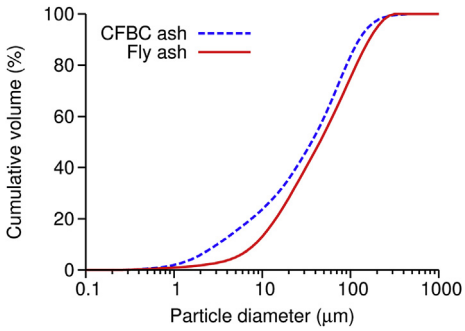

Fig. 2. Cumulative volume of conventional and CFBC fly ashes.

Table 1
Chemical composition of conventional and CFBC fly ashes (wt. %).

	SiO_2	Al_2O_3	Fe_2O_3	CaO	K_2O	TiO_2	SO_3
CFBC ash	31.4	26.2	4.9	21.9	0.4	5.5	8.0
Fly ash	52.4	35.0	5.1	1.8	2.1	1.5	0.2

Table 2
Quantitative XRD phase analysis of raw materials. Mass fractions (wt %).

	Lime	Conventional fly ash	CFBC fly ash
Amorphous content	10.9	60.6	54.9
Calcite	26.4		2.2
Portlandite ($Ca(OH)_2$)	62.8		1.7
Mullite		33.3	
Quartz		6.2	7.5
Anhydrite			13.5
Hematite			4.9
Free lime (CaO)			11.1
Rutile			1.1
Fairchildite			3.0

Table 3
Mix compositions of the ternary binder (wt. %).

	CFBC fly ash	Conventional fly ash	$Ca(OH)_2$	Water	Superplasticizer
Paste from TB	0.313	0.313	0.094	0.263	0.017

database. Zincite was added as an internal standard to quantify the amorphous content [23].

Thermal gravimetric analysis was carried out by M. Palkovská, Institute of Inorganic Chemistry ASCR, on a SetSys Evolution 1750 device. A synthetic air atmosphere (Messer) was employed and the heating rate was set to 10°C/min.

Helium pycnometry was carried out by H. Šnajdaufová, Institute of Chemical Process Fundamentals (ICPF) ASCR, on a Micrometrics AccuPyc 1330 pycnometer.

SEM images and EDX analyses were collected by Ch. Rößler, FIB Bauhaus Universität Weimar, on a scanning electron microscope of type Nova NanoSEM 230 (FEI) equipped with a field emission gun (Shottky emitter) and various detectors for imaging (secondary electron detectors, SE; backscattered electron detectors, BSE) and analysis (EDX-Silicon Drift Detector, EDAX/Ametek Pegasus XM4 with Genesis 6.35 software) were used for this investigation. For SEM-EDX mappings, the samples were embedded in epoxy resin and mechanically polished with a diamond slurry up to 0.25 μm. An electrically conductive coating of a few nanometers of carbon was applied to the polished surfaces. The following EDX mapping conditions have been applied: acceleration voltage 12.0 kV, approximately 9000 cps, 512 × 400 pixel mapping resolution (approx. 1 μm/pixel), dead time of EDX detector was always below 30%. Phase analysis on EDX mappings was carried out with the software package Genesis 6.35 (EDAX/Ametek). The word phase thereby refers to an area of the sample with a similar chemical composition.

In a first run an automated phase cluster analysis (PCA) was carried out to check which phases could be differentiated. The PCA compares the full spectrum at each point in a map to identify the phases. The first pass through the PCA uses blocks of pixels. It compares the average spectrum in these blocks (each 2 × 2 pixels in the present study). If two blocks differ more than the amount defined by the tolerance (χ^2 fit), then they are assumed to belong to separate phases. This procedure is followed for each block and then repeated so that each pixel is assigned to a given phase. The obtained phases were validated by manually checking the composition of the phases found on the samples against the phase composition found in the cluster analysis. In this way, it is assured that the mean phase composition is as close as possible to an expected phase. The number of detected phases is partly reduced by combining phases of similar composition (i.e. variation in chemical composition of fly ashes is not displayed). Determined average phase compositions were saved in a phase library and applied to all investigated samples. Four mappings of each sample are recorded and analysed (total mapped area approx. 0.2 mm^2). Thus, mean phase content and standard deviation are obtained on four mappings.

3. Results

3.1. XRD analysis

Table 4 presents the results of XRD-Rietveld analysis on the hydrated samples; the X-ray diffractograms are depicted in Fig. 3. Eight phases are distinguished using the XRD, namely quartz, ettringite, mullite, calcite, portlandite ($Ca(OH)_2$), anhydrite, hematite, and (indirectly using the addition of a Zincite internal standard) an amorphous content. The amorphous content is expected to consist of two general phases, i.e. the glassy phase originating from the conventional fly ash, and the C-S-H gel which is formed during the hydration. Since the two phases could not be easily distinguished using the XRD approach, a thermal gravimetric analysis is proposed to access the C-S-H gel fraction.

Table 4
Quantitative XRD phase analysis of TB pastes at 3, 7, 28 and 60 days of curing. Mass fractions (wt %). Densities of the crystalline phases are obtained from Ref. [24], density of amorphous content calculated from measured bulk density, porosity, and the known densities of crystalline phases.

	Density (g/cm3)	0D	3D	7D	28D	60D
Amorphous content	2.0	51	56	62	51	58
Quartz	2.7	6	5	5	5	6
Ettringite	1.8	0	2	3	16	12
Mullite	3.3	14	15	14	13	13
Calcite	2.7	4	4	4	5	5
Portlandite ($Ca(OH)_2$)	2.3	15	11	7	6	3
Anhydrite	3.0	6	3	1	0	0
Hematite	5.3	4	4	4	4	3

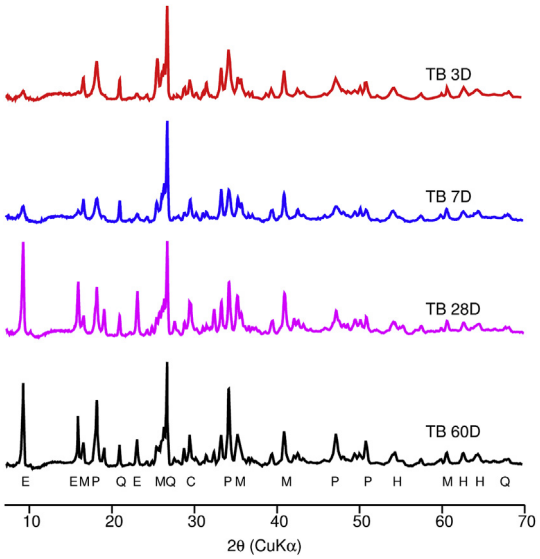

Fig. 3. X-ray diffractograms of TB pastes at 3, 7, 28 and 60 days of curing. Legend: E-ettringite; M-mullite; P-portlandite; H-hematite; Q-quartz; C-calcite.

3.2. DTG analysis

The main goal of the DTG analysis lies in C-S-H gel quantification. This is done using deconvolution of the total mass loss during the DTG analysis to assess contributions of ettringite, C-S-H gel, $Ca(OH)_2$ and $CaCO_3$.

The first question is the amount of ettringite. Data on thermal decomposition of ettringite can be found in Ref. [25] or in a recent book [26]. The ettringite is usually referred to as a crystalline phase containing 30–32 mol of H_2O. However, an extensive drying procedure to a zero relative humidity causes loss of water, and formation of an X-ray amorphous metaettringite with 9–12 mol of

H_2O [27]. Fig. 4 shows DTG curves of both ettringite and metaettringite. The relative mass loss reads 45% (wt.) for ettringite and 20% (wt.) for metaettringite respectively.

Since the TB paste was acetone + vacuum dried prior to the DTG measurements, a comparative analysis on a virgin sample (no drying or hydration cessation) is proposed to identify the effect of the drying procedure to a possible ettringite transformation. Fig. 5 shows both DTG curves for dried and virgin sample. In the case of the virgin sample, the first peak around 70°Cis related to natural humidity within the sample. For the temperature range of 100–750°C, both DTG curves are nearly identical, which demonstrates that ettringite was not transformed by the acetone + vacuum drying procedure and no metaettringite was formed.

The thermal decomposition progress of $Ca(OH)_2$ and $CaCO_3$ is calibrated on raw materials, see Fig. 6. The decomposition of portlandite,

$$Ca(OH)_2 \rightarrow CaO + H_2O, \quad (1)$$

occurs around 450°C. The peak of calcite decomposition,

$$CaCO_3 \rightarrow CaO + CO_2, \quad (2)$$

was found around 750°C. The dehydration of C-S-H gel occurs in a broad peak between 100 and 400°C [28], and the composition of C-S-H gel is assumed as [29].

$$1.7CaO \cdot SiO_2 \cdot 1.3H_2O. \quad (3)$$

The relative mass losses are calculated from molar weights of corresponding phases, e.g. for $Ca(OH)_2$, Eq. (1):

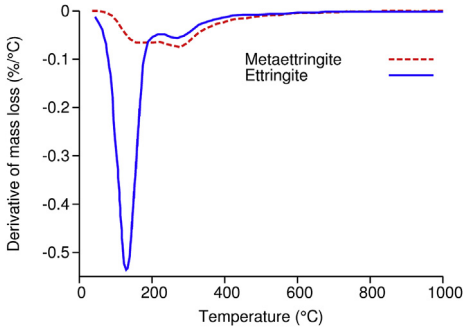

Fig. 4. Derivative of mass loss of ettringite and metaettringite, data from Ref. [25].

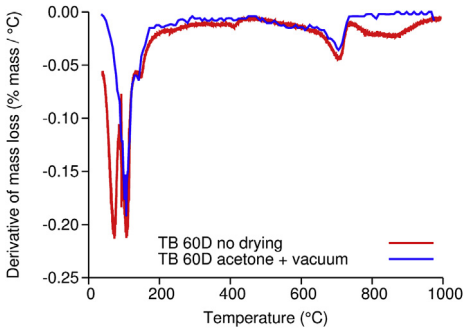

Fig. 5. Comparison of DTG curves after 60 days of sealed curing of TB paste. Paste dried using acetone + vacuum approach and paste without any drying prior to the DTG analysis.

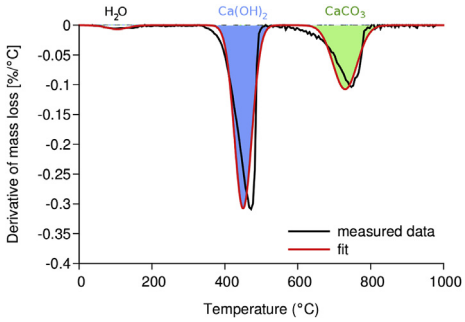

Fig. 6. Derivative of mass loss of $Ca(OH)_2$ and $CaCO_3$, DTG.

$$m_r = \frac{M_{H_2O}}{M_{Ca(OH)_2}} = \frac{18.015}{74.092} = 0.24. \quad (4)$$

Table 5 summarizes the expected relative mass losses of the four particular phases: ettringite, C-S-H gel, $Ca(OH)_2$ and $CaCO_3$. No other phases are identified from the DTG analysis, however a potential carbonate phase occurs in the deconvolution around 650°C. Omission of this phase has no effect on the identified amount of C-S-H gel, which is the main task of the DTG analysis.

Since the deconvolution of the DTG curves has a relatively large number of degrees of freedom, a unique solution does not exist. The deconvolution proposed in Fig. 8 and Table 6 is done with respect to the results from XRD analysis in Table 4. Fig. 7 shows mass of the TB paste samples during heating from 30 °Cto 1000°C.

Table 5
Thermal decomposition of ettringite, C-S-H, $Ca(OH)_2$ and $CaCO_3$. Relative mass loses and corresponding peak temperatures.

	Approx. peak temperature	Mass loss (wt.)		
Ettringite	120°C	45% →	(H_2O)	[25]
C-S-H	150°C	13% →	(H_2O)	Eq. (3), [28]
$Ca(OH)_2$	450°C	24% →	(H_2O)	Eq. (1)
$CaCO_3$	750°C	44% →	(CO_2)	Eq. (2)

Table 6
Mass fractions from DTG analysis. Quantitative phase analysis of TB pastes at 3, 7, 28 and 60 days of curing, (wt %).

	3D	7D	28D	60D
Ettringite	3	5	14	14
C-S-H	28	39	42	42
$Ca(OH)_2$	5	5	5	4
$CaCO_3$	5	5	5	5

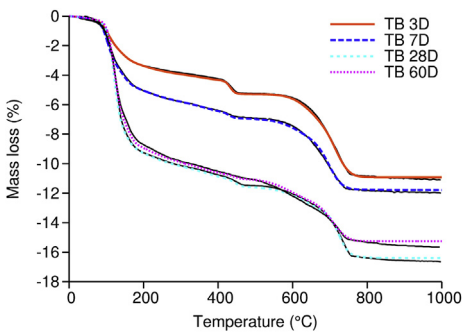

Fig. 7. Mass loss (TG) of TB pastes at 3, 7, 28 and 60 days of curing.

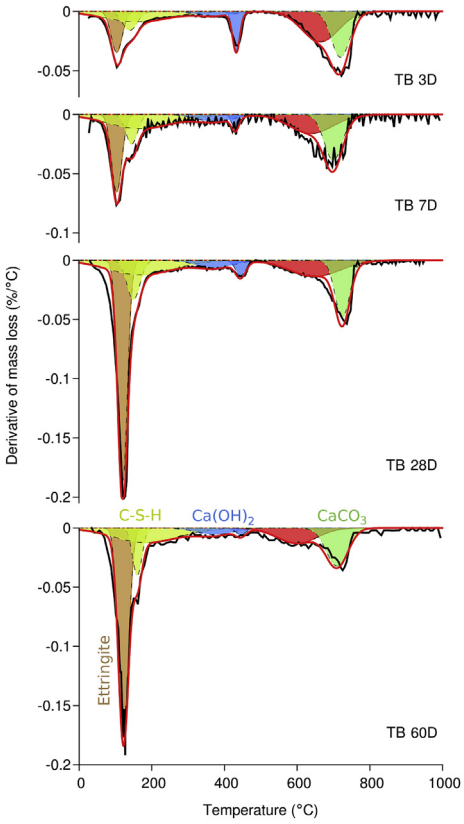

Fig. 8. Differential thermal gravimetry of TB pastes at 3, 7, 28 and 60 days of curing. Derivative of mass loss. Proposed fit of particular phases using Gaussian curves.

3.3. Porosity assessment

Two types of porosities are here distinguished. Gel pores with a nominal diameter under 3 nm in the C-S-H gel, and capillary pores above [30]. The volume of entrapped air is neglected. Total porosity corresponds to the sum of gel and capillary porosities. Immediately after the mixing, the total porosity corresponds to the water volume in the fresh paste, see Tables 3 and 7.

Porosity on matured TB paste stems from skeletal density $\rho_{skeletal}$ obtained from He pycnometry and the measured bulk density ρ_{bulk} from volume and mass of vacuum-dried samples as

$$\phi = 1 - \frac{\rho_{bulk}}{\rho_{skeletal}}. \quad (5)$$

Since He pycnometry is used to obtain $\rho_{skeletal}$ and the He molecules are smaller than the nominal diameter of the gel pores, the porosity obtained from Eq. (5) is considered as the total.

Table 7
Total porosity, bulk density ρ_{bulk} and skeletal density $\rho_{skeletal}$ of TB paste. ρ_{bulk} from mass/volume measurements on vacuum-dried samples; $\rho_{skeletal}$ from He pycnometry. Total porosity is calculated from Eq. (5), average and standard deviation from three samples are mentioned.

	0D	3D	7D	28D	60D
ρ_{bulk} (g/cm^3)	1.71[A]	1.30	1.36	1.38	1.40
$\rho_{skeletal}$ (g/cm)	–	2.30	2.23	2.28	2.25
Total porosity	0.48±0.01[B]	0.43±0.02	0.39±0.02	0.39±0.02	0.38±0.01

[A]Water saturated state;[B]Volume of water in the fresh mixture.

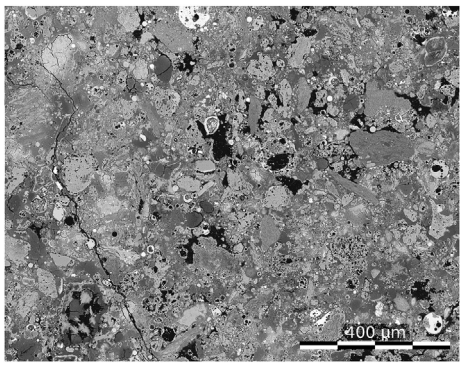

Fig. 9. Merged image containing 20 backscattered SEM images of TB paste after 60 days of curing. Magnification 1000×, scanned area 1.5 mm^2.

3.4. SEM imaging, EDX analysis

Scanning electron microscopy (SEM) backscattered image analysis was proposed as a tool for quantification of the volumetric fractions of particular individual phases. See Fig. 9 for a large image assembled from 20 SEM scans with 1000x magnification (total scanned area 1.5 mm^2). The particular phases appear as different peaks in the computed gray level histogram, see Fig. 10. The C-S-H matrix, ettringite and the unreacted fly ash can be hardly distinguished and quantified separately from the histogram, thus an energy-dispersive X-ray spectroscopy (EDX) is proposed as an efficient tool for quantification of the volume phases.

Polished sections of 7 and 60 days old TB samples are analysed in terms of EDX mapping, see Fig. 11. Four main phases are identified in the EDX analysis: 1. matrix hydrates (mainly C-S-H and some finely intergrown hydrates such as ettringite, AFm etc.), 2. calcium hydroxide/carbonate, 3. ettringite/AFm, 4. porosity, see Table 8. The ettringite crystals as well as hydration products and unreacted fly ash particles are visible under SEM-SE on fractured surface of the TB paste, see Fig. 12.

3.5. Model of volumetric phase evolution

The model of volumetric phase evolution is constructed from measured total porosity, mass fractions from XRD, and mass fractions from deconvoluted DTG curves. The SEM/EDX results are only indicative. Seven phases are distinguished in the volumetric model: capillary pores, C-S-H gel consisting of C-S-H globules and gel pores, ettringite, amorphous glass, calcium hydroxide, and non-

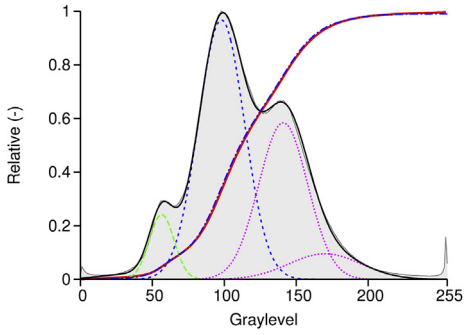

Fig. 10. Gray level histogram of BSE-SEM image of 60 days old TB paste from Fig. 9 with proposed phase deconvolution. Left peak corresponds to visible porosity, middle peak to a matrix with unreacted fly ash, right peak mainly to fly ash particles and unreacted CFBC.

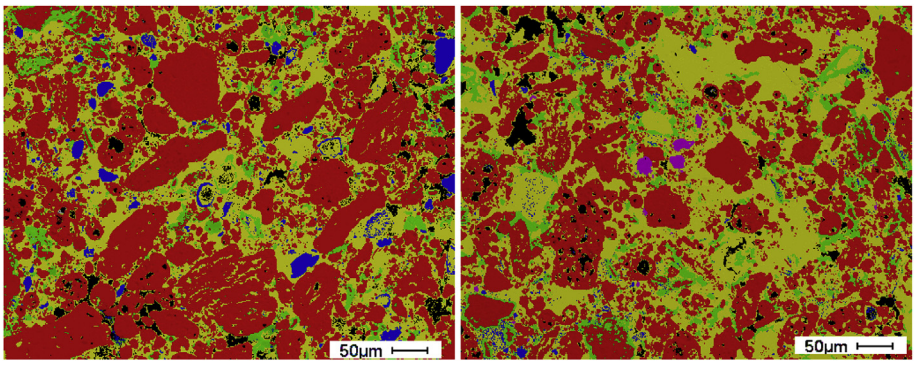

Fig. 11. EDX mapping of TB paste after 7 days (left) and 60 days (right) of sealed curing. Color legend: yellow - matrix hydrates, green - ettringite/AFm, black - porosity, blue - $Ca(OH)_2$, $CaCO_3$, red - fly ash, violet - iron rich particles. (For interpretation of the references to colour in this figure legend, the reader is referred to the Web version of this article.)

Table 8
Quantitative EDX analysis of TB paste at 7 and 60 days of sealed curing and proposed quantification of phases identified from the grey value analysis of BSE image. Average volume fractions from four measurements (EDX) and 1.5 mm^2 (SEM) (vol. %).

	EDX 7D	EDX 60D	SEM 60D
Fly ash	55	45	41
Matrix hydrates	30	42	51
Large pores	4	3	8
$Ca(OH)_2/CaCO_3$	4	1	–
AFt/AFm	6	8	–

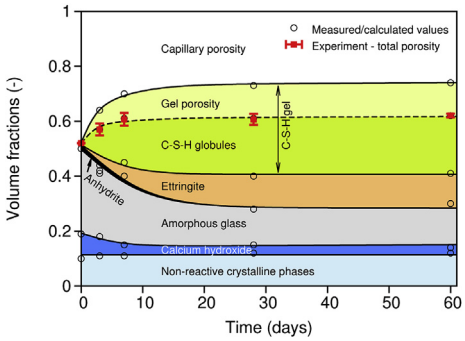

Fig. 13. Volumetric model of phase evolution during hydration of ternary binder.

reactive crystalline phases.

The total porosity is directly identified from Table 7. The amount of non-reactive crystalline phases, calcium hydroxide and total amorphous content originates from XRD analysis; the amount of ettringite and C-S-H gel comes from DTG deconvolutions, see Tables 4 and 6. The identified mass fractions are recalculated to volume fractions using known densities of the particular phases, and normalized to 100% volume (without total porosity). The density of C-S-H globules is assumed as 2.25 g/cm^3 for a globule with 1.3 mol H_2O (compare Eq. (3), no evaporable water) [31]. The density of amorphous glass is fitted, so the theoretical calculated bulk density from the volumetric model corresponds to the measured one. The density is identified as 2.0 g/cm^3.

The total measured porosity in Table 7 is divided into the capillary and the gel contributions. The fraction of C-S-H-gel pores is derived from the identified volume of C-S-H gel using its characteristic porosity 0.37 (for a LD C-S-H gel with a packing density 0.63) [31,32]. The rest of the measured total porosity is aligned to the capillary porosity.

Fig. 13 shows the proposed volumetric model of phase evolution during hydration of the ternary binder. The measured/calculated data for 0, 3, 7, 28 and 60 days of curing are shown and a smooth monotonic fit is proposed.

3.6. Compressive strength prediction

Compressive strength evolution is generally governed by the

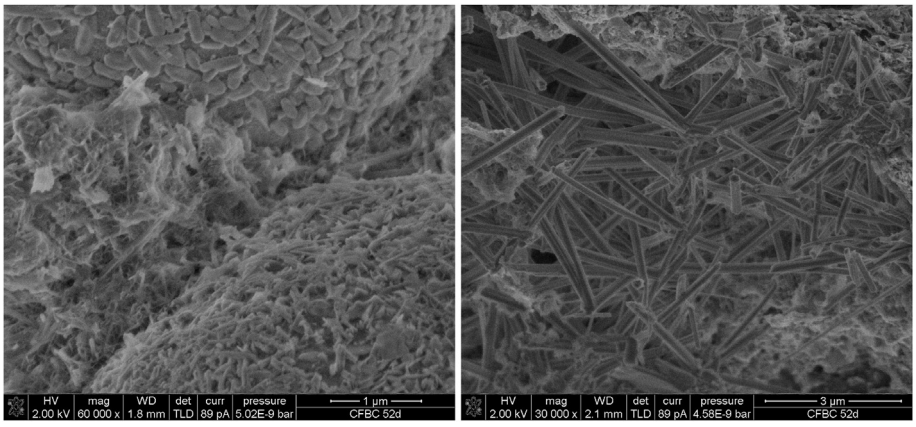

Fig. 12. SEM-SE of TB paste after 52 days of sealed curing, fractured surface with visible hydration products and unreacted fly ash particle (left) and ettringite crystals (right).

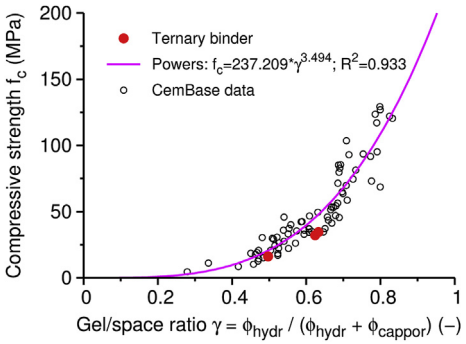

Fig. 14. Compressive strength of ternary binder with regards to OPC and blended cements in the form of gel/space descriptor.

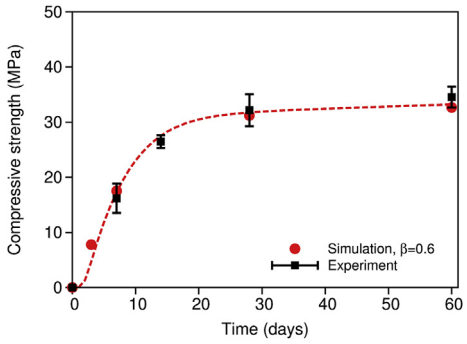

Fig. 16. Evolution of compressive strength of ternary binder.

weakest solid percolating phase in a microstructure, which has been linked to a gel in Portland cement-based materials. Therefore, the gel/space ratio belongs to a traditional descriptor coined by Powers [20] and TB can be tested for this hypothesis as well. Fig. 14 shows the relationship with CemBase, a public database [33] devoted mainly to microstructure characterization of ordinary and blended Portland cement pastes, often complemented with compressive strength and elastic moduli. It contains mix designs for 83 pastes and 27 mortars, covering water/binder ratios of 0.16–0.69. The ternary binder in Fig. 14 exhibits a slight underestimation which points to an inappropriate gel descriptor, i.e. gel composed of C-S-H and ettringite.

As has been shown recently, C-S-Hgoverns the evolution of compressive strength on OPC and blended cement pastes as the weakest solid percolating phase, see Fig. 15 [20]. This alternative descriptor in the form of C-S-H/space ratio shows that this ternary binder comes exactly on the average predicted value of the multiscale micromechanical model with $\beta = 0.6$. It becomes evident that ettringite does not contribute substantially to the compressive strength since including ettringite into the gel deviates more from empirical fit in Fig. 14.

Detailed evolution of compressive strength evolution is depicted in Fig. 16 using standard parameters for the micromechanical model such as cohesive strength of C-S-H globule as 320 MPa. It signalizes a formation of characteristic C-S-H gel as found within Portland cement-based pastes.

The coexistence between C-S-H and ettringite seems not to be detrimental since both products evolve simultaneously during 28 days. This is in contrast with the crystallization pressure of delayed ettringite formation which causes cracking of a mature C-S-H matrix, due to limited creep capacities.

This hypothesis of simultaneous growth explains why CFBC ash alone causes significant expansion due to ettringite formation. Fig. 13 shows that ettringite forms 12.2% vol. for TB at 60 days while CFBC ash alone would yield approximately 30% vol., too much for absorption within forming C-S-H. Therefore, the conventional fly ash has two roles in the ternary blend; decrease amount of forming ettringite by reducing CFBC content and provide additional C-S-H due to pozzolanic reaction.

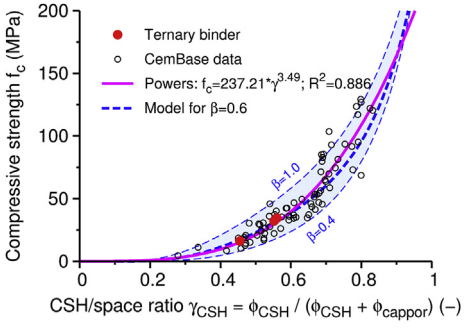

Fig. 15. Compressive strength of ternary binder with regards to OPC and blended cements in the form of C-S-H/space descriptor.

4. Conclusion

A ternary binder synthesized from CFBC fly ash, conventional fly ash, and calcium hydroxide exhibits hydraulic properties resulting in 32 MPa compressive strength after 28 days of curing. The binder utilizes CFBC fly ash, which is otherwise unsuitable for OPC blending due to its high sulfur content and free CaO. The ternary binder could be used for low-demanding applications such as soil stabilizations, void fillings, temporary road constructions, etc.

For a deeper understanding in the microstructure-strength links, the evolution of phase volumes is determined using a combination of XRD, TGA, SEM and porosimetry. A multiscale micromechanical model provides a good validation of the compressive strength evolution with standard model parameters derived from Portland cement-based binders.

Acknowledgement

The authors gratefully acknowledge financial support from Czech Science Foundation under the project 16-20008S.

References

[1] J. Brandštetr, J. Havlica, I. Odler, Properties and use of solid residue from fluidized bed coal combustion, in: S. Chandra (Ed.), Waste Materials Used in Concrete Manufacturing, William Andrew Publishing, Westwood, NJ, 1996, pp. 1–52.
[2] E.J. Anthony, D.L. Granatstein, Sulfation phenomena in fluidized bed combustion systems, Prog. Energy Combust. Sci. 27 (2) (2001) 215–236.
[3] E.J. Anthony, L. Jia, Y. Wu, CFBC ash hydration studies, Fuel 84 (11) (2005) 1393–1397.
[4] S. Rajaram, Next generation CFBC, Chem. Eng. Sci. 54 (22) (1999) 5565–5571.
[5] P. Basu, Combustion of coal in circulating fluidized-bed boilers: a review, Chem. Eng. Sci. 54 (22) (1999) 5547–5557.
[6] J. Koornneef, M. Junginger, A. Faaij, Development of fluidized bed combustion—An overview of trends, performance and cost, Prog. Energy Combust. Sci. 33 (1) (2007) 19–55.
[7] J. Havlica, J. Brandštetr, I. Odler, Possibilities of utilizing solid residues from pressured fluidized bed coal combustion (PSBC) for the production of blended cements, Cement Concr. Res. 28 (2) (1998) 299–307.
[8] P. Chindaprasirt, S. Thaiwitcharoen, S. Kaewpirom, U. Rattanasak, Controlling ettringite formation in FBC fly ash geopolymer concrete, Cement Concr. Compos. 41 (2013) 24–28.
[9] P. Chindaprasirt, U. Rattanasak, C. Jaturapitakkul, Utilization of fly ash blends from pulverized coal and fluidized bed combustions in geopolymeric materials, Cement Concr. Compos. 33 (1) (2011) 55–60.
[10] Q. Li, H. Xu, F. Li, P. Li, L. Shen, J. Zhai, Synthesis of geopolymer composites

from blends of CFBC fly and bottom ashes, Fuel 97 (2012) 366–372.
[11] Z. Zhang, J. Qian, C. You, C. Hu, Use of circulating fluidized bed combustion fly ash and slag in autoclaved brick, Construct. Build. Mater. 35 (2012) 109–116.
[12] Y. Xia, Y. Yan, Z. Hu, Utilization of circulating fluidized bed fly ash in preparing non-autoclaved aerated concrete production, Construct. Build. Mater. 47 (2013) 1461–1467.
[13] C.S. Shon, D. Saylak, D.G. Zollinger, Potential use of stockpiled circulating fluidized bed combustion ashes in manufacturing compressed earth bricks, Construct. Build. Mater. 23 (5) (2009) 2062–2071.
[14] M. Illikainen, P. Tanskanen, P. Kinnunen, M. Körkkö, O. Peltosaari, V. Wigren, et al., Reactivity and self-hardening of fly ash from the fluidized bed combustion of wood and peat, Fuel 135 (2014) 69–75.
[15] Xg Li, Qb Chen, Kz Huang, Bg Ma, B. Wu, Cementitious properties and hydration mechanism of circulating fluidized bed combustion (CFBC) desulfurization ashes, Construct. Build. Mater. 36 (2012) 182–187.
[16] G. Sheng, Q. Li, J. Zhai, F. Li, Self-cementitious properties of fly ashes from CFBC boilers co-firing coal and high-sulphur petroleum coke, Cement Concr. Res. 37 (6) (2007) 871–876.
[17] L. Armesto, J. Merino, Characterization of some coal combustion solid residues, Fuel 78 (5) (1999) 613–618.
[18] G. Sheng, Q. Li, J. Zhai, Investigation on the hydration of CFBC fly ash, Fuel 98 (2012) 61–66.
[19] R.B. Jewell, R.F. Rathbone, T.Y. Duvallet, T.L. Robl, K.C. Mahboub, Fabrication and testing of low-energy calcium sulfoaluminate-belite cements that utilize circulating fluidized bed combustion by-products, Coal Combustion and Gasification Products 7 (2015) 9–18.
[20] M. Hlobil, V. Šmilauer, G. Chanvillard, Micromechanical multiscale fracture model for compressive strength of blended cement pastes, Cement Concr. Res. 83 (2016) 188–202.
[21] T.C. Powers, Structure and physical properties of hardened Portland cement paste, J. Am. Ceram. Soc. 41 (1) (1958) 1–6.
[22] V. Šmilauer, P. Hlaváček, F. Škvára, R. Šulc, L. Kopecký, J. Němeček, Micromechanical multiscale model for alkali activation of fly ash and metakaolin, J. Mater. Sci. 46 (20) (2011) 6545–6555.
[23] R.E. Dinnebier, S.J. Billinge, Powder Diffraction: Theory and Practice, Royal society of chemistry, 2008.
[24] J.H. Bernard, R. Rost, et al., Encyklopedický Přehled Minerálů, Academia, Praha, 1992.
[25] L.G. Baquerizo, Impact of Water Activity on the Mineralogy of Hydrated Cement [Thèse No. 6487], EPFL, Lausanne, 2015.
[26] K. Scrivener, R. Snellings, B. Lothenbach, A Practical Guide to Microstructural Analysis of Cementitious Materials, CRC Press, 2016.
[27] L.G. Baquerizo, T. Matschei, K.L. Scrivener, Impact of water activity on the stability of ettringite, Cement Concr. Res. 79 (2016) 31–44.
[28] E. Stepkowska, J. Blanes, F. Franco, C. Real, J. Pérez-Rodrıguez, Phase transformation on heating of an aged cement paste, Thermochim. Acta 420 (1) (2004) 79–87.
[29] H.F.W. Taylor, Cement Chemistry, Academic Press, New York, 1990.
[30] A.M. Neville, Properties of Concrete, John Wiley & Sons, Inc., 1997.
[31] H.M. Jennings, Refinements to colloid model of C-S-H in cement: CM-II, Cement Concr. Res. 38 (3) (2008) 275–289.
[32] G. Constantinides, F.J. Ulm, The nanogranular nature of C-S-H, J. Mech. Phys. Solid. 55 (2007) 64–90.
[33] V. Šmilauer, M. Hlobil, CemBase - Database for Ordinary and Blended Cement Pastes and Mortars, Version 2016-10-20, Czech Technical University in Prague, Thákurova 7, 166 29 Prague 6, 2016. http://mech.fsv.cvut.cz/~smilauer/.